Available online at www.sciencedirect.com
ScienceDirect
International Journal of Heat and Mass Transfer 50 (2007) 4698–4712
International Journal of HEAT and MASS TRANSFER
www.elsevier.com/locate/ijhmt

Numerical studies on an air-breathing proton exchange membrane (PEM) fuel cell

Y. Zhang, R. Pitchumani *

Advanced Materials and Technologies Laboratory, Department of Mechanical Engineering, University of Connecticut, Storrs, CT 06269-3139, United States

Received 8 November 2006; received in revised form 5 March 2007
Available online 14 June 2007

Abstract

The objective of this article is to investigate the performance of an air-breathing proton exchange membrane (PEM) fuel cell operating with hydrogen fed at the anode and air supplied by natural convection at the cathode. Considering a dual-cell cartridge configuration with a common anode flow chamber, a comprehensive two-dimensional, non-isothermal, multi-component numerical model is developed to simulate the mass transport and electrochemical phenomena governing the cell operation. Systematic parametric studies are presented to investigate the effects of operating conditions, cell orientation and cell geometry on the performance. Temperature and species distributions are also studied to assist the understanding of the single cell performance for different conditions. It is shown that the cell orientation affects the local current density distribution along the cell and the average current density, particularly at lower cell voltages. The cell performance is shown to improve with increase of temperature, anode flow rate, anode pressure and anode relative humidity.

Keywords: Proton exchange membrane (PEM) fuel cell; Air breathing; Numerical model; Fuel cell orientation; Passive fuel cell

1. Introduction

Fuel cells are considered as promising candidates of alternative power sources, in which chemical energy is directly converted into electricity. Since water is the only product if pure hydrogen is fed, fuel cells offer high efficiency and emission-free operation. Over the last decade, proton exchange membrane (PEM) fuel cells have gained much attention since they can operate at low temperatures, start up quickly and yield high power density. These characteristics make PEM fuel cells attractive in many applications including automotive, distributed power generation, and portable electronic devices. However, the high manufacturing cost and low reliability and durability of fuel cells have severely limited their widespread commercialization.

The drive to understand the complex and interrelated transport and electrochemical phenomena inside PEM fuel cells has resulted in many numerical simulations and experimental tests being reported in the literature. The earlier work on fuel cell modeling can be traced back to Springer et al. [1] and Bernardi and Verbrugge [2], who developed one-dimensional, isothermal, steady-state models for PEM fuel cells by assuming perfect membrane hydration. More recently, the one-dimensional models have been extended to studying water and thermal management [3], carbon monoxide (CO) poisoning [4] and optimization of operating conditions [5]. The modeling rigor has also grown to include two-dimensional effects [6], transient operation [7], three-dimensional modeling [8–11], and two-phase flow and transport [12,13].

There has also been much interest in developing passive PEM fuel cells designs, which eliminate or reduce the balance of plant such as fans, compressors, etc., and are ideally targeted for portable, light weight applications and as either replacement for batteries or use as hybrid systems [14,15]. One version of the passive design is an air-breathing PEM fuel cell which is exposed to the atmosphere on the cathode side and draws air for its operation entirely

* Corresponding author. Tel.: +1 860 486 0683; fax: +1 860 486 5088.
E-mail address: pitchu@engr.uconn.edu (R. Pitchumani).

0017-9310/$ - see front matter © 2007 Elsevier Ltd. All rights reserved.
doi:10.1016/j.ijheatmasstransfer.2007.03.044

Nomenclature

a	water vapor activity
A	fuel cell active area [m^2]
c_f	fixed charged site concentration in membrane [mol/m^3]
c_p	specific heat at constant pressure [J/kg/K]
D_i	diffusivity of species i [m^2/s]
E_{cell}	cell voltage [V]
F	Faraday's constant [C/mol]
$\vec{g}$	gravity vector [m^2/s]
$\hat{\mathbf{i}}, \hat{\mathbf{j}}$	unit vectors in x and y-directions
i	local current density [A/m^2]
I	magnitude of the local current density vector [A/m^2]
I_{ave}	average current density [A/m^2]
$\vec{i}_{local}$	local current density vector [A/m^2]
j	exchange current density [A/m^3]
k	permeability of porous media or equivalent porous media [m^2]
k_ϕ	electrokinetic permeability of membrane [m^2]
k_t	thermal conductivity [w/m/K]
L	fuel cell length along the hydrogen chamber [m]
M_i	molecular weight of species i [kg/s]
m	flow rate [lpm]
p	pressure [Pa]
p_{sat}	saturation pressure of water vapor [bar]
RH	relative humidity
S	source terms of governing equations
T	temperature [K]
$\vec{V}$	superficial velocity vector [m/s]
V	volume [m^3]
x	position co-ordinate across the cell thickness/the membrane
x_i	mole fraction of species i
y_i	mass fraction species i
y	position co-ordinate along the chamber
z_f	charge of sulfonate site in the membrane

Greek symbols

α	transfer coefficient
ε	porosity
ε_{mc}	volume fraction of membrane in the catalyst layer
η	surface over potential [V]
λ	water content
ρ	fluid density [kg/m^3]
σ	electrical/protonic conductivity [1/ohm/m]
$\vec{\tau}$	the stress tensor [$kg/m^2/s^2$]
ϕ	phase potential [V]

Subscripts

a	anode
ave	average
c	cathode
eff	effective value
f	fluid phase
H_2	hydrogen
i	species
m	membrane phase
O_2	oxygen
ref	reference
s	solid phase
w	water
x, y	component in the x- and y- directions

Superscript

eff	effective value

through natural convection. Several experimental studies have been reported on the performance and design of air-breathing PEM fuel cells. Schmitz et al. [16] investigated the influence of cathode opening area and wetting properties of diffusion layers on the cell performance; effects of cathode structure including different gas diffusion layers and current collectors were investigated in [17]; an alternative design employing adhesive copper film as anode current collector and a gold-plated stainless steel mesh combined with the current collector cut out from a printed circuit board on the cathode side was reported in [18]; design and fabrication of micro air-breathing fuel cells based on micromachining and micropatterning technologies were developed in [19,20].

While the above-mentioned studies report experimental feasibility and prototype demonstrations of air-breathing fuel cells, relatively few numerical simulations for such cells are available. A theoretical analysis combined with experimental tests on the feasibility and restrictions of feeding oxygen by natural convection was developed in [21]. Mennola et al. [22] presented a two-dimensional modeling for the cathode gas diffusion layer and gas channel to study the limiting processes of mass transport inside the cell. A two-dimensional, isothermal, steady-state mathematical model was developed and supported by experimental tests in [23] to study the influence of the cathode opening area on the cell performance. Ziegler et al. [24] extended Schmitz's two-dimensional model [23] to include non-isothermal effects. Transport phenomena governing species distributions, potential distributions and temperature distribution were investigated and the effects of ribs on the cathode frame were also evaluated. Recently, Ying et al. [25,26] presented a three-dimensional model and corresponding experimental work to investigate the air-breathing cell performance and the effects of ambient conditions and channel configurations on the performance. The

detailed species-electrochemical transports were investigated in [27], along with the effects of overpotential on the fluid flow, mass transport and electrochemistry. Also, the transport phenomena in a free-breathing cathode of a printed-circuit-board (PCB)-based fuel cell were studied numerically in [28]. Parametric studies were used to investigate the influence of the breathing-hole diameter and the cathode-layer thickness on the cell performance.

The goal of the present study is to investigate a new design for an air-breathing PEM fuel cell. The design consists of two single fuel cells flanking and sharing a common hydrogen chamber on their anode sides to form a cartridge. The two individual cells in the cartridge derive oxygen on the exposed cathode sides from atmospheric air in a passive way by natural convection and diffusion. Several cartridges may be stacked in an array and connected either in series or parallel to obtain the desired power and performance requirements. Considering this design, the paper presents a computational study of the performance of a single cell. A two-dimensional, non-isothermal model is developed and validated with experimental data. The validated model is, in turn, used in a parametric exploration of the effects of cell orientation, operating conditions and cell geometry on the overall performance as well as the detailed flow species, temperature and current density distributions inside the cell. The following section describes the mathematical model underlying the computational simulations and the results from the simulations are presented in Section 3.

2. Mathematical model

The fuel cell cartridge considered in the study consists of two single cells sharing a common hydrogen flow chamber on their anode sides, while the cathode sides of the two cells are exposed to ambient air. Fig. 1 shows an exploded view of a cartridge. Each cell in the cartridge comprises a layered structure of seven components as identified in one of the cells in Fig. 1: (1) an outermost frame with ribs to provide overall support; (2) an anode metal mesh which acts as anode current collector; (3) an anode gas diffusion layer; (4) a membrane electrode assembly (MEA), consisting of a proton transport membrane and two catalyst layers on its surfaces where electrochemical reactions take place; (5) a cathode gas diffusion layer; (6) a cathode metal mesh which acts as cathode current collector; and (7) a common anode hydrogen flow chamber shared by the two cells, with designed flow passage to maximize hydrogen fuel availability across the cell plane. The component layers of the two cells are bolted together to form a cartridge. The two individual cells can be connected in parallel or series to meet the design requirements. The frames and the metal meshes serve to increase the stiffness of the cartridge and minimize the deformation of the fuel cell, and correspondingly decrease the interfacial contact resistances inside the cell.

A schematic illustration of a two-dimensional cross section of the assembled cartridge spanning across the thickness of the cell (x-direction) and along the length of the hydrogen chamber (y-direction), as considered in the modeling, is shown in Fig. 2a. Note that although the hydrogen flow in the chamber may be three dimensional in an actual cell due to the serpentine flow path way, the present study simplifies it as a single channel extending along the length of the cell. Owing to the large hydrogen diffusivity, this simplification is expected to be reasonably accurate for the studies in this work. Furthermore, the effects of the frame and the ribs are not considered in this modeling, but may be readily incorporated in a future extension of the work. By virtue of symmetry along the midline of the hydrogen chamber, the computational modeling is based on the half domain of the cartridge, identified in Fig. 2b.

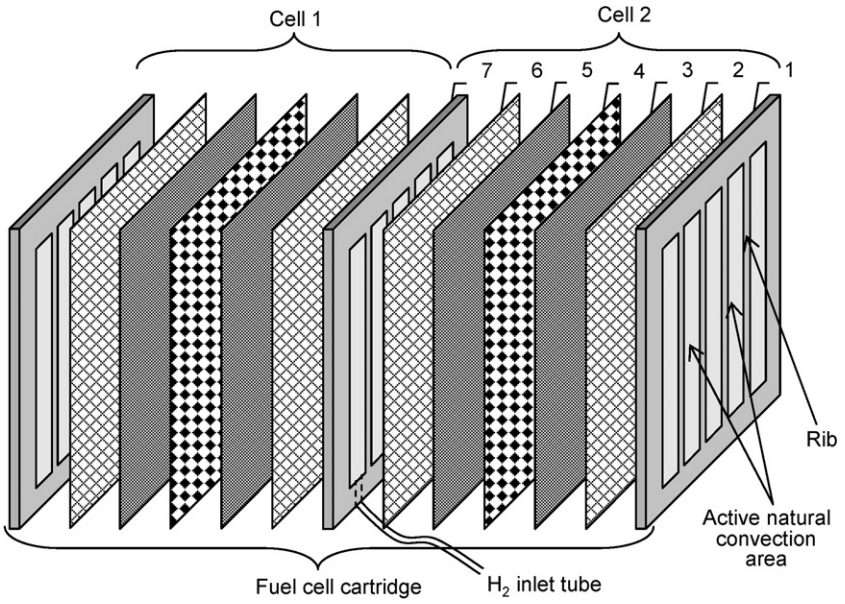

Fig. 1. Illustration of an air-breathing PEM fuel cell cartridge.

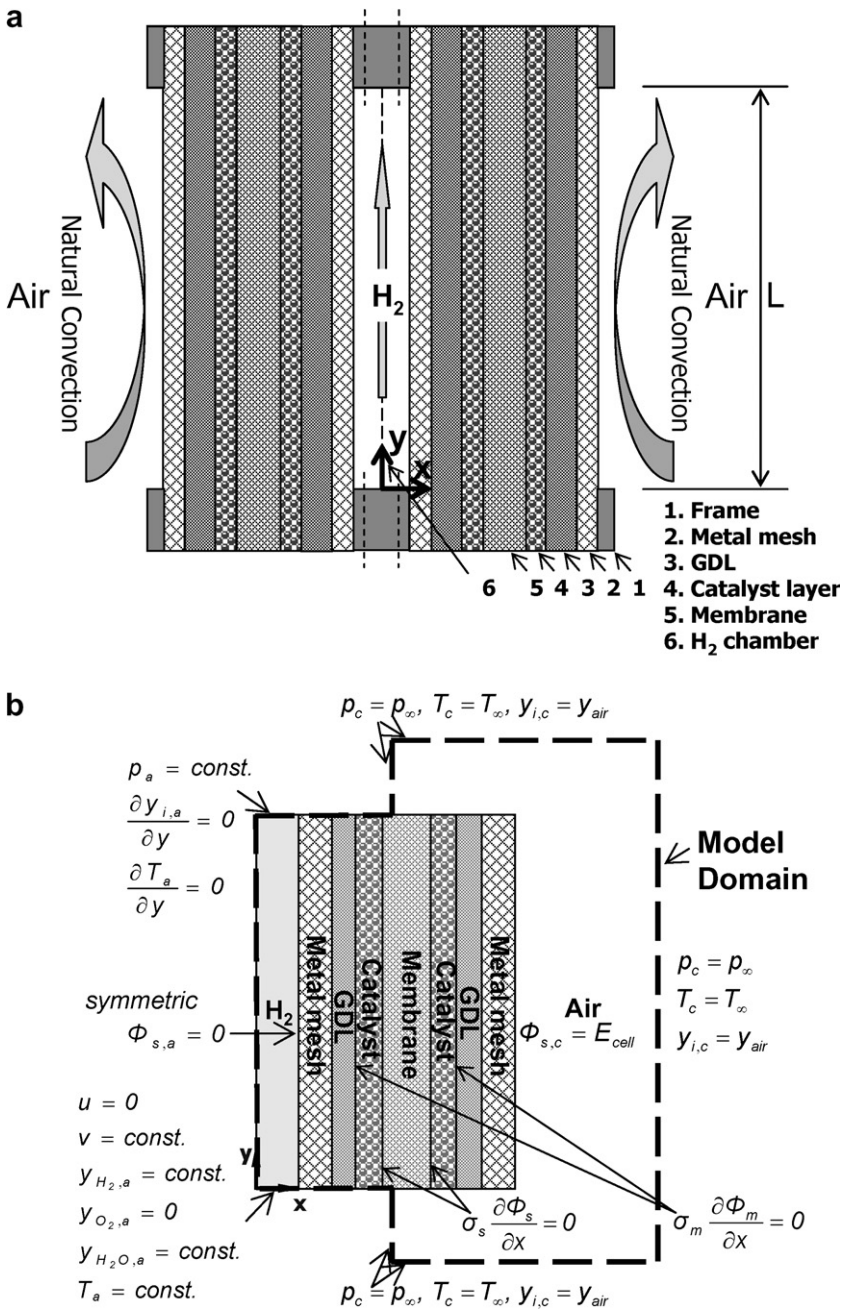

Fig. 2. Schematic of (a) a two-dimensional cross section along the length and thickness of an air-breathing PEM fuel cell cartridge and (b) the model domain and the associated boundary conditions.

During the operation of the cartridge, hydrogen gas (H_2) is supplied into the flow chamber at a constant flow rate, transfers through the metal mesh and gas diffusion layer, and arrives at the anode catalyst sites where it is dissociated to protons and electrons. Protons are transported with water inside the fuel cell across the MEA to the cathode side, while electrons transport in the opposite direction through the gas diffusion layer, metal mesh and external circuitry to the cathode catalyst layer. At the cathode, the required oxygen (O_2) is drawn into the cell from the ambient air by natural convection and diffusion and reacts with protons and electrons at the cathode catalyst layer, generating water. The computational modeling is developed here based on the previous study [29] to describe the governing physical phenomena. The gas transport through the domain is governed by the coupled continuity, momentum, and species conservation equations; the water transport from anode to cathode is modeled as source terms representing the electroosmotic drag, and is included in the momentum equations for the catalyst layers and the membrane. Since water is transported from the anode to the cathode and also generated at the cathode catalyst layer, water concentration on the cathode side is generally large and greatly affects the mixture density, which, in turn,

affects the natural convection flow. The electron transport is governed by solid phase potential equation in the catalyst, gas diffusion layers and metal mesh at anode and cathode sides, while the proton transport is expressed as membrane phase potential equation in the two catalyst layers and the membrane, in which the electrochemical reactions contribute as the source terms based on the Butler-Volmer expressions. The heat released from the electrochemical reactions and Joule heating are included in the energy equation to solve for the temperature distribution inside the cell and in the ambient air around the cell, which drives the natural convection flow over the cell.

The assumptions underlying the present model follow those routinely adopted in the previous studies, namely: (1) the species are treated to be ideal gas mixtures; (2) the flow is assumed as laminar in the entire model domain; (3) liquid water is not considered due to the relatively low current density characteristic of air-breathing cells in comparison to conventional PEM fuel cells with forced cathodic flow; (4) the gas diffusion layers, catalyst layers and membrane are considered to be isotropic and homogeneous; (5) the membrane is considered impermeable to gas flow and crossover phenomena is not considered; (6) contact resistances are not considered; and (7) Joule heating is only considered in the membrane and catalyst layers. The coupled system of governing equations presented here is formulated to describe the entire half-domain with the phenomena specific to each region expressed in terms of appropriate source terms. This provides a unified formulation as summarized below with specific source terms listed in Table 1.

The conservation of mass is governed by the continuity equation for compressible fluids with sink/source terms, S_c, to account for species consumptions/generations:

$$\nabla \cdot (\rho \vec{V}) = S_c \tag{1}$$

where ρ is the fluid mixture density, $\vec{V}$ is the superficial velocity vector or volume-averaged velocity vector with components u in the x-direction and v in the y-direction to ensure the mass flux continuity at the interface of porous media and non-porous media. The source term S_c representing the mass consumption/generation due to the reactions is coupled with the current generation and only exists in the two catalyst layers.

The phenomena of the mixture fluid transport inside the fuel cell and the oxygen transport into the fuel cell by natural convection of air are described by the conservation of momentum equations with specific source terms, S_V, in the various regions. Gravity effect, which causes the natural convection flow outside the cartridge under temperature difference, only exists along the vertical direction. The gas diffusion layers, the metal mesh, the catalyst and the membrane regions are considered as porous media for the species transport with their corresponding porosity and permeability values. The metal mesh is treated as anisotropic with a finite permeability across it thickness and zero permeability in its plane. The electroosmotic force is also included to describe the transport of protons and water in the MEA from anode to cathode [6]. The momentum equation accounting for all the above effects can be written as

$$\nabla \cdot (\rho \vec{V} \vec{V}) = -\nabla p + \nabla \cdot \vec{\tau} + \rho \vec{g} + S_V \tag{2}$$

where p is the pressure, $\vec{\tau}$ is the stress tensor, $\vec{g}$ is gravity vector, which is 0 m/s^2 in the horizontal direction and 9.8 m/s^2 in the vertical direction. The source term S_V is expressed in Table 1 and comprises only pressure gradient due to flow through porous media in the gas diffusion layers and metal mesh layers and includes both pressure gradient due to flow through porous media and electroosmotic drag in the MEA. In the expression for S_V, ε_{eff} is the porosity or equivalent porosity in the corresponding regions. The fluid mixture density, ρ, is calculated based on the ideal gas law as a function of temperature and pressure: $\rho = p/R_{\text{mix}}T$, where R_{mix} is the specific gas constant of the mixture, defined as the ratio of the Universal gas constant to the mixture molec-

Table 1
Source terms in the governing equations for the various regions of the fuel cell

Region	S_c	S_V	S_T	S_i		S_s, S_m
Gas channels	0	0	0	0		0
Diffusion layers and metal meshes	0	$-\frac{\mu}{k}\varepsilon_{\text{eff}}\vec{V}$	0	0		0
Catalyst layers	Anode: $-\frac{j_a}{2F}M_{H_2}$	$-\frac{\mu}{k_p}\varepsilon_{\text{eff}}\vec{V}+\frac{k_\phi}{k_p}z_f c_f F\nabla\phi_m$	Anode: $j_a\eta_a+\frac{i^2}{\sigma_m^{\text{eff}}}$	Anode: $-\frac{j_a}{2F}M_{H_2}$	(H_2)	Anode:
				0	(O_2)	
				0	(H_2)	$S_s=-j_a>0$
						$S_m=+j_a<0$
	Cathode: $-\frac{j_c}{4F}M_{O_2}+\frac{j_c}{2F}M_{H_2O}$		Cathode: $-j_c\eta_c+\frac{i^2}{\sigma_m^{\text{eff}}}$	Cathode: 0	(H_2)	Cathode:
				$-\frac{j_c}{4F}M_{O_2}$	(O_2)	
				$\frac{j_c}{2F}M_{H_2O}$	(H_2O)	$S_s=+j_c>0$
						$S_m=-j_c<0$
Membrane	0	$-\frac{\mu}{k_p}\varepsilon_{\text{eff}}\vec{V}+\frac{k_\phi}{k_p}z_f c_f F\nabla\phi_m$	$\frac{i^2}{\sigma_m^{\text{eff}}}$	0		0

ular weight, $R_{\text{mix}} = R/M_{\text{mix}} = R/\sum(x_i Mi)$, where x_i is the mole fraction of species in the mixture and M_i is the molecular weight of the corresponding species.

Electrochemical reactions occur in the two catalyst layers of the MEA causing a heat release and a temperature increase in the cell. Furthermore, Joule heating is considered in the MEA due to its low electrical conductivity. The temperature gradient in the ambient air in the vicinity of the cell surface drives the natural convection flow under the buoyancy effect that is responsible for the feed of oxygen at the cathode governed by the term $\rho\vec{g}$ in Eq. (2). Heat transport and exchange between the solid phase and the fluid phase in porous media can be solved by two methods: local thermal non-equilibrium approach described in [30–32] and equilibrium approach described in [33]. Here, local thermal equilibrium approach is applied to solve for the phase-averaged temperature:

$$\nabla \cdot (\rho c_p \vec{V} T) = \nabla \cdot (k_{\text{t}}^{\text{eff}} \nabla T) + S_T \tag{3}$$

where c_p is fluid mixture specific heat at constant pressure. $k_{\text{t}}^{\text{eff}}$ is the effective thermal conductivity, which can be expressed as follows in the porous media [33]:

$$k_{\text{t}}^{\text{eff}} = \varepsilon_{\text{eff}} k_{\text{t,f}} + (1 - \varepsilon_{\text{eff}}) k_{\text{t,s}} \tag{4}$$

where the terms $k_{\text{t,f}}$ and $k_{\text{t,s}}$ are the thermal conductivities of the fluid and solid, respectively; and S_T is the heat generated in the catalyst layers due to reactions and Joule heating in the MEA. Since the electrical conductivity of the solid carbon is much larger compared with its ionic conductivity, Joule heating generated in the solid phase is neglected.

The species are transported inside the fuel cell by diffusion and advection, and react on the surfaces of the catalyst, causing H_2 and O_2 to be consumed and water and current to be generated. The transport and reactions of species are described by the species conservation equations:

$$\nabla \cdot (\rho \vec{V} y_i) = \nabla \cdot (\rho D_i^{\text{eff}} \nabla y_i) + S_i \tag{5}$$

where y_i represents the ith species mass fraction, source term S_i represents the consumption of H_2 in the anode catalyst layer, and the consumption of O_2 and generation of H_2O in the cathode catalyst layer, as shown in Table 1. The effective diffusivity of individual species D_i^{eff} in the porous media is modeled using the Bruggeman correlation, based on the effects of porosity and empirical dependence of tortuosity on the porosity in the porous media [34]:

$$D_i^{\text{eff}} = \varepsilon_{\text{eff}}^{1.5} D_i \tag{6}$$

where D_i is the diffusivity of individual species i, expressed as a function of temperature T and pressure p [34]:

$$D_i = D_{i,\text{ref}} \left(\frac{T}{T_{\text{ref}}}\right)^{1.5} \left(\frac{p_{\text{ref}}}{p}\right) \tag{7}$$

in which, $D_{i,\text{ref}}$ is the diffusivity of the species i at the reference temperature and pressure: $T_{\text{ref}} = 353$ K and $p_{\text{ref}} = 1$ atm, listed in Table 2. For pure H_2 supply, the subscript i denotes four components (1) H_2, (2) O_2, (3) H_2O and (4) N_2. Three components, $y_1 = y_{H_2}$, $y_2 = y_{O_2}$ and $y_3 = y_{H_2O}$, are obtained by solving the species equations corresponding to Eq. (5), and the fourth component, $y_4 = y_{N_2}$, is calculated by:

$$y_4 = 1 - \sum_{i=1}^{3} y_i \tag{8}$$

Protons and electrons are generated through dissociation of H_2 in the anode catalyst. Protons transported through the membrane and electrons transported toward the cathode through external circuitry react with oxygen at the cathode catalyst and produce current and water. The conduction of electrons in the solid region and protons through the membrane is governed by two Poisson equations for the solid phase and membrane phase potentials, ϕ_{s} and ϕ_{m}, respectively, as follows:

$$\nabla \cdot (\sigma_j^{\text{eff}} \nabla \phi_j) + S_j = 0; \quad j = s, m \tag{9}$$

where subscripts s and m denote the solid phase and the membrane phase, respectively, ϕ_j denotes the corresponding phase potential, σ_j, $j = s, m$, are the effective electrical conductivities, and the source terms S_j, $j = s, m$, are expressed by the transfer current densities as listed in Table 1. The effective electrical conductivity of solid phase, $\sigma_{\text{s}}^{\text{eff}}$, is expressed as a function of the effective porosity, ε_{eff}, and the electrical conductivity of the solid material σ_{s}:

$$\sigma_{\text{s}}^{\text{eff}} = (1 - \varepsilon_{\text{eff}}) \sigma_{\text{s}} \tag{10}$$

The effective membrane ionic conductivity in the catalyst layers can be expressed as

$$\begin{aligned} \sigma_{\text{m}}^{\text{eff}} &= \varepsilon_{\text{mc}}^{1.5} \sigma_{\text{m}} \\ &= \varepsilon_{\text{mc}}^{1.5} (0.5139\lambda - 0.326) \exp\left[1268\left(\frac{1}{303} - \frac{1}{T}\right)\right] \end{aligned} \tag{11}$$

where ε_{mc} is membrane volume fraction in the catalyst layer, and the ionic conductivity in the membrane phase σ_{m} is expressed as the function of temperature, T, and the hydration parameter, λ, defined as water molecules per sulfonate group, in the membrane [1]. The hydration parameter, λ, can be estimated by the following empirical expression [1], such that a value of λ larger than 14 indicates the presence of over-saturated water vapor in the membrane:

$$\lambda = \begin{cases} 0.043 + 17.81a - 39.85a^2 + 36.0a^3 & 0 \leqslant a \leqslant 1 \\ 14 + 1.4(a - 1) & 1 \leqslant a \leqslant 3 \end{cases} \tag{12}$$

where a is water vapor activity, expressed as $a = x_{\text{w}} p / p_{\text{sat}}$, in which, x_{w} is water mole fraction, and p_{sat} is the temperature-dependent saturation pressure of water [1]:

$$\begin{aligned} \log p_{\text{sat}} = &-2.1794 + 0.02953(T - 273.15) \\ &- 9.1837 \times 10^{-5} (T - 273.15)^2 \\ &+ 1.4454 \times 10^{-7} (T - 273.15)^3 \end{aligned} \tag{13}$$

Table 2
Physical and geometry parameters used in the numerical simulations

Parameter	Symbol	Value	Source [Ref.]
Length of H_2 chamber (cm)	L	1.68/5.00	Experiments
Metal mesh (screen) width (mm)		0.5	
Gas diffusion width (mm)		0.3	
Catalyst layer width (mm)		0.016	
Membrane width (mm)		0.018	
H_2 chamber width (mm)		3.2	
Permeability of diffusion layer (m^2)	k	2.97×10^{-9}	Experiments
Gas diffusion porosity	ε	0.776	
Anode reference exchange current density (A/m^3)	$J_{a,ref}$	1.0×10^8	
Cathode reference exchange current density (A/m^3)	$j_{c,ref}$	3000	
Hydraulic permeability of membrane (m^2)	K_p	1.58×10^{-18}	[6]
Electrokinetic permeability (m^2)	K_ϕ	1.13×10^{-19}	
H_2O viscosity in the membrane (kg/(m s))	μ_{H_2O}	8.91×10^{-4}	
Anode/cathode transfer coefficient	α_a/α_c	0.5/2.0	
Fixed site charge	Z_f	−1	
Membrane water porosity	ε_m	0.28	
Volume fraction membrane in catalyst layer	ε_{mc}	0.5	
Fixed charge concentration ($kmol/m^3$)	C_f	1.2	
H_2 diffusivity in catalyst layer and membrane (m^2/s)	$D_{H_2,cata}$	2.59×10^{-10}	[39]
H_2 diffusivity in gas (m^2/s)	$D_{H_2,ref}$	1.1×10^{-4}	
O_2 diffusivity in gas (m^2/s)	$D_{O_2,ref}$	3.2×10^{-5}	
H_2O diffusivity in gas (m^2/s)	$D_{H_2O,ref}$	7.35×10^{-5}	
O_2 diffusivity in catalyst layer and membrane (m^2/s)	$D_{O_2,cata}$	8.328×10^{-10}	[35]
Thermal conductivity of screen mesh (w/(m k))		91.7	[4]
Thermal conductivity of carbon (w/(m k))		1.3	
Thermal conductivity of catalyst layer (w/(m k))		1.0	
Thermal conductivity of membrane (w/(m k))		0.24	

where the saturation pressure, p_{sat}, is in bar, and the temperature, T, is in K.

The volumetric source terms in the potential equations, S_j, $j = s, m$, only exist in the two catalyst layers where electrochemical reactions occur, and are determined by the exchange current densities, j_a and j_c, which are governed by the Butler-Volmer equations [8]:

$$j_a = j_{a,ref}\left(\frac{x_{H_2}}{x_{H_2,ref}}\right)^{0.5}\left[\exp\left(\frac{\alpha_a F}{RT}\eta_a\right) - \exp\left(-\frac{\alpha_a F}{RT}\eta_a\right)\right] \tag{14}$$

$$j_c = j_{c,ref}\left(\frac{x_{O_2}}{x_{O_2,ref}}\right)\left[\exp\left(\frac{\alpha_c F}{RT}\eta_c\right) - \exp\left(-\frac{\alpha_c F}{RT}\eta_c\right)\right] \tag{15}$$

In the above equations, subscripts a and c denote anode and cathode, respectively, j_{ref} is the reference volumetric exchange current density, α is the charge transfer coefficient, x_{H_2} and x_{O_2} are the mole fractions of H_2 and O_2 in the catalyst layers, F is the Faraday constant, and η is the surface over potential defined as [7]:

$$\eta = \phi_s - \phi_m - E_{ref} \tag{16}$$

where E_{ref} is taken to be 0 at the anode and equals the temperature-dependent open cell voltage, $E_{OC} = 0.0025T + 0.2329$, on the cathode side, where the temperature, T is in K [35].

The local current density vector can be written as $\vec{i}_{local} = i_x\hat{\mathbf{i}} + i_y\hat{\mathbf{j}}$, where i_x denotes the component in the x-direction and i_y denotes the component in the y-direction. Each of these components is, in turn, expressed as the sum of the current due to the proton transport ($i_{m,x}$, $i_{m,y}$) and that due to electron transport ($i_{s,x}$, $i_{s,y}$). The electronic current is obtained as the product of the effective electronic conductivity and the electronic potential gradient and likewise, the protonic current is given by the product of the effective protonic conductivity and the protonic potential gradient. The components of the current density are, therefore, expressed as

$$i_x = i_{s,x} + i_{m,x} = -\sigma_s^{eff}\frac{\partial\phi_s}{\partial x} - \sigma_m^{eff}\frac{\partial\phi_m}{\partial x} \tag{17}$$

$$i_y = i_{s,y} + i_{m,y} = -\sigma_s^{eff}\frac{\partial\phi_s}{\partial y} - \sigma_m^{eff}\frac{\partial\phi_m}{\partial y} \tag{18}$$

The local current density, I_{local}, is defined as the magnitude of the local current density vector, which is expressed as follows:

$$I_{local} = |\vec{i}_{local}| = \sqrt{i_x^2 + i_y^2} \tag{19}$$

The average current density of the fuel cell, I_{ave}, can be calculated by integrating the local current density over the planar area, which is also equivalent to the integration of the exchange current densities over the entire volume of the catalyst layer, and division by the planar area, A, as

$$I_{ave} = \frac{1}{A}\int \vec{i}_{local}\cdot \mathrm{d}A = \frac{1}{A}\int j_a\,\mathrm{d}\mathbf{V} = \frac{1}{A}\int j_c\,\mathrm{d}\mathbf{V} \tag{20}$$

The polarization curve is constructed by solving for the average current density, I_{ave}, for different values of cell voltage, E_{cell}, which is set as a boundary condition at the cathode surface in the solution of the solid phase potential equation.

The simulation domain, illustrated in Fig. 2b, is constructed from the mid-line of the hydrogen chamber to a certain ambient region on the cathode side. The boundary conditions for the ambient region, shown as the dashed lines on the right side in Fig. 2b, are set as follows: the cathode pressure, p_c, cathode temperature, T_c, and cathode species mass fractions, $y_{i,c}$, equal those in the atmosphere. The dimensions of the ambient air region in the model domain were chosen based on numerical studies on varying the dimensions until the size was large enough to approximate the ambient boundary conditions without altering the simulation results. The air domain size was determined to be a function of the cell dimensions in that a larger cell required a larger air domain in the simulations. The dimensions of the ambient air domain for the specific cases discussed in this paper are indicated in the following section on presentation of results. The left boundary condition at the midline of the hydrogen chamber is assumed symmetric due to geometry symmetry and negligible gravity effect in the forced flow of hydrogen in different orientations. The interface conditions at any two adjacent layers in the domain are implicitly satisfied since the governing equations are formulated and implemented for the entire region as a single domain. Therefore, the boundary conditions for the solid potential equation, which is equal to zero at the interface of the hydrogen chamber and the metal mesh and is equal to cell voltage, E_{cell}, at the cathode surface, are extended to the outer left and right borders of the domain with infinite electrical conductivity in the hydrogen chamber region and in the extended ambient region. Since there is no proton transport outside the MEA, the boundary conditions for the membrane phase potential are zero proton flux at the interfaces of the catalyst layers and gas diffusion layers, which is implemented as zero ionic conductivity in the regions except the MEA. Furthermore, the boundary conditions at hydrogen inlet are: specified velocity components, u, v, specified humidified hydrogen, $y_{H_2,a}$, $y_{H_2O,a}$, specified anode temperature, T_a, while those at the hydrogen outlet are as follows: specified anode pressure, p_a, and zero gradients for other flow quantities. All the above boundary conditions are shown in Fig. 2b.

The fuel cell simulation model described by the equations presented in this section was implemented in a commercial finite-volume based computational fluid dynamics solver, *Fluent*, using the physical and geometry parameters listed in Table 2. Several user-written subroutines were embedded to describe mass consumption/generation, heat generation, water transport, electrochemical reactions and the potential equations as well as the effective properties for specific regions. A segregated implicit method was used to solve the coupled governing equations and the semi-implicit method for pressure-linked equations consistent (SIMPLEC) algorithm [36] was used for pressure correction to ensure mass conservation. Expressions for the effective coefficients, properties and the specific source terms were implemented as external subroutines and interfaced with the Fluent software as user defined functions. A non-uniform mesh comprising a total of 5748 grids was used, which was found to yield convergence in the results to within 2%. The coupled set of governing equations was solved iteratively to a convergence criterion that the maximum scaled residual of all the variables being solved is less than 10^{-6}. The numerical simulations were used to explore the cell performance over a range of parameters and the results of the study are presented in the following section.

3. Results and discussion

The numerical simulation model was validated with experimental data to establish the accuracy of the simulations. Fig. 3 presents the comparisons of polarization curves in terms of the cell voltage, E_{cell}, as a function of the average current density, I_{ave}. The numerical simulation results are denoted by the solid lines, and the experimental data [37] are indicated by the solid markers for different operating conditions and geometry parameters. The basic operating conditions in these studies on passive operation of air-breathing fuel cells are as follows: temperature at the anode, $T_a = 298$ K, atmosphere pressure at the anode, $p_a = 1$ atm, and zero anode relative humidity for hydrogen flow, $RH_a = 0$, while the operating conditions at the cathode are set to be the same as those in the atmosphere. The orientation of the cell is such that gravity acts parallel to the cell length in the negative y-direction, referred to as the vertical orientation. The predicted polarization curve from numerical simulations is compared with experimental data for two different cell lengths, L, along the y-direction in Fig. 2a: $L = 1.68$ cm (active area $= 9$ cm^2) and $L = 5.0$ cm (active area $= 25$ cm^2), under the conditions of anode temperature, anode pressure, and hydrogen stream humidification, as shown in Fig. 3a–d. It is seen that the cell voltage, E_{cell}, decreases monotonically with increase of the average current density, I_{ave}, owing to the ohmic, activation and concentration losses. A comparison of the data in Fig. 3a–b reveals that increasing hydrogen flow temperature at the anode slightly improves the cell performance since the temperature inside the cell slightly increases, correspondingly reducing the activation loss and increasing species diffusivity which, in turn, improves the species transport. The enhanced anode relative humidity from 0 (dry hydrogen) in Fig. 3b to 1 (fully humidified hydrogen) in Fig. 3c increases the water content in the membrane, leading to higher ionic conductivity and lower ohmic loss in the membrane, and results in higher average current density at the same cell voltages. However, comparing Fig. 3a with Fig. 3d, it is seen that extending fuel cell length reduces the average current density since exposure of the fuel cell surface at the cathode to fresh oxygen from atmosphere diminishes along the length, leading to ineffective utilization of the active fuel cell area. Overall, the model predictions in the four plots show a close agreement with experimental data to within a maximum of 7%, which forms a reliable basis for the use of the present numerical

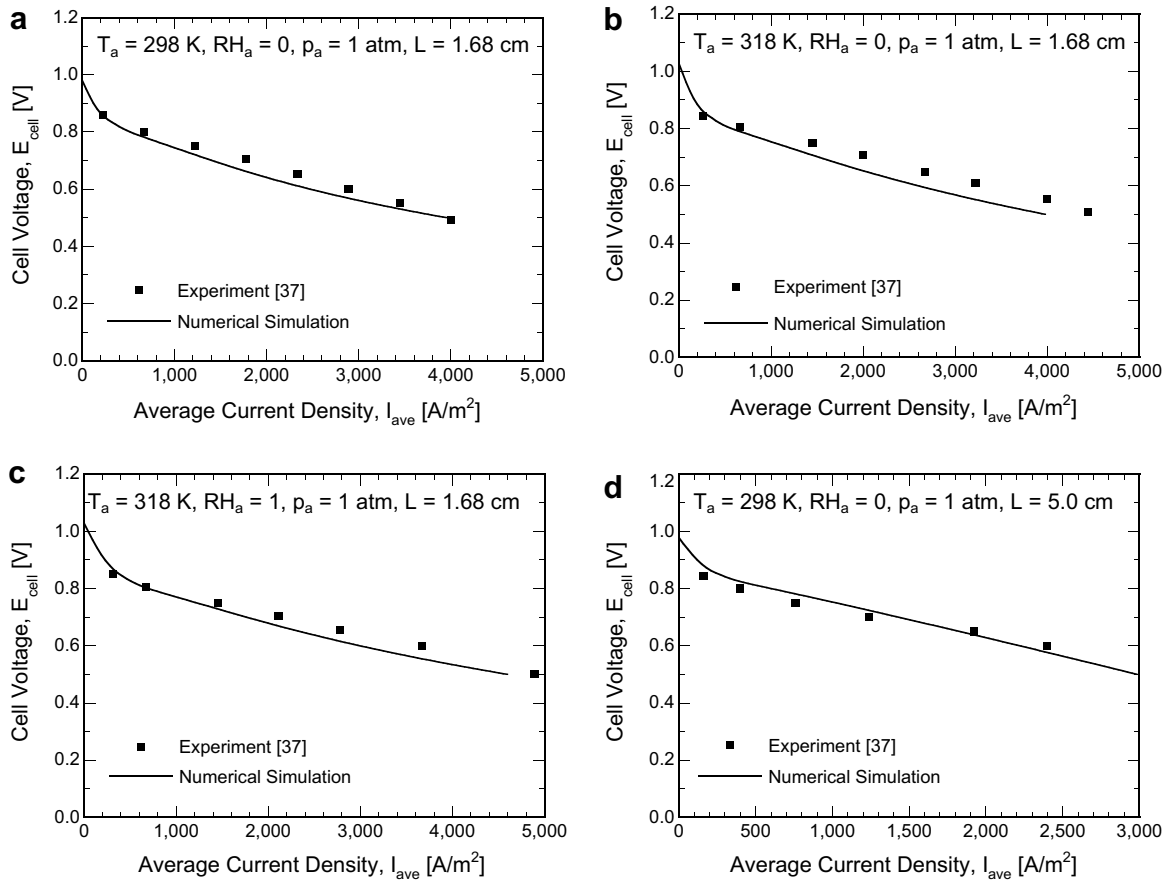

Fig. 3. Validation of the numerical simulations with experimental polarization curve data under four different operating conditions as indicated in the plots.

model to conduct systematic studies on the interrelated phenomena inside fuel cells.

For better understanding of the natural convection phenomenon around the fuel cell, Fig. 4 provides temperature contours and stream lines in the modeling domain at $E_{cell} = 0.5$ V for two sizes of fuel cells in three different orientations: (a) vertical, in which gravity acts in the negative y-direction, (b) horizontal upward, in which gravity acts in the negative x-direction, and (c) horizontal downward, in which gravity acts in the positive x-direction. The temperature contours, represented by the gray scale, and the stream lines, represented by the solid lines with arrows to describe the flow patterns, are shown in Fig. 4a–c for the small cell ($L = 1.68$ cm) in the vertical, horizontal upward and horizontal downward orientations, respectively, while those for the large cell ($L = 5.0$ cm) in the three orientations are shown in Fig. 4d–f. The dimensions of the ambient air domain used in the simulation of the two different cell sizes are also shown in Fig. 4a–f. From Fig. 4a–c, it is observed that the temperature distributions inside the fuel cell are not significantly different for the three orientations; the temperature increases quickly from 298 K at the inlet of the hydrogen chamber to the maximum temperature, 304 K. Fig. 4g presents the temperature distribution across the mid-length of the small cell in the horizontal upward orientation. It is shown that the peak temperature (identified in Fig. 4g) occurs on the cathode side due to the significant kinetic loss for the oxygen reduction reaction. It is seen that the temperature variation inside the cell is very small, around 1 K, indicating that heat generation due to the electrochemical reactions and Joule heating due to current transport are not significant owing to the small current density and the rapid heat conduction in the solid regions of the cell. In the ambient region outside the cell, the temperature drops back to the value of 298 K, with a total cell-to-ambient temperature variation of 6 K as shown in Fig. 4g. The flow patterns and the temperature distributions outside the fuel cell for the three different orientations are consistent with those for natural convection around heated flat boards [38]: the fuel cell in the vertical orientation draws fresh air from the bottom, and the air rises along the length of the cell as it gets heated and simultaneously exchanges mass with the cell (Fig. 4a); in the horizontal upward configuration (Fig. 4b), air is drawn symmetrically from the lateral sides of the cell, gets heated and exchanges mass as it passes over the cell surface and rises up from the center of the cell length as shown in Fig. 4b; in the horizontal downward orientation, air is drawn from beneath the cathode surface of the cell, flows symmetrically along the cell surface while exchanging mass

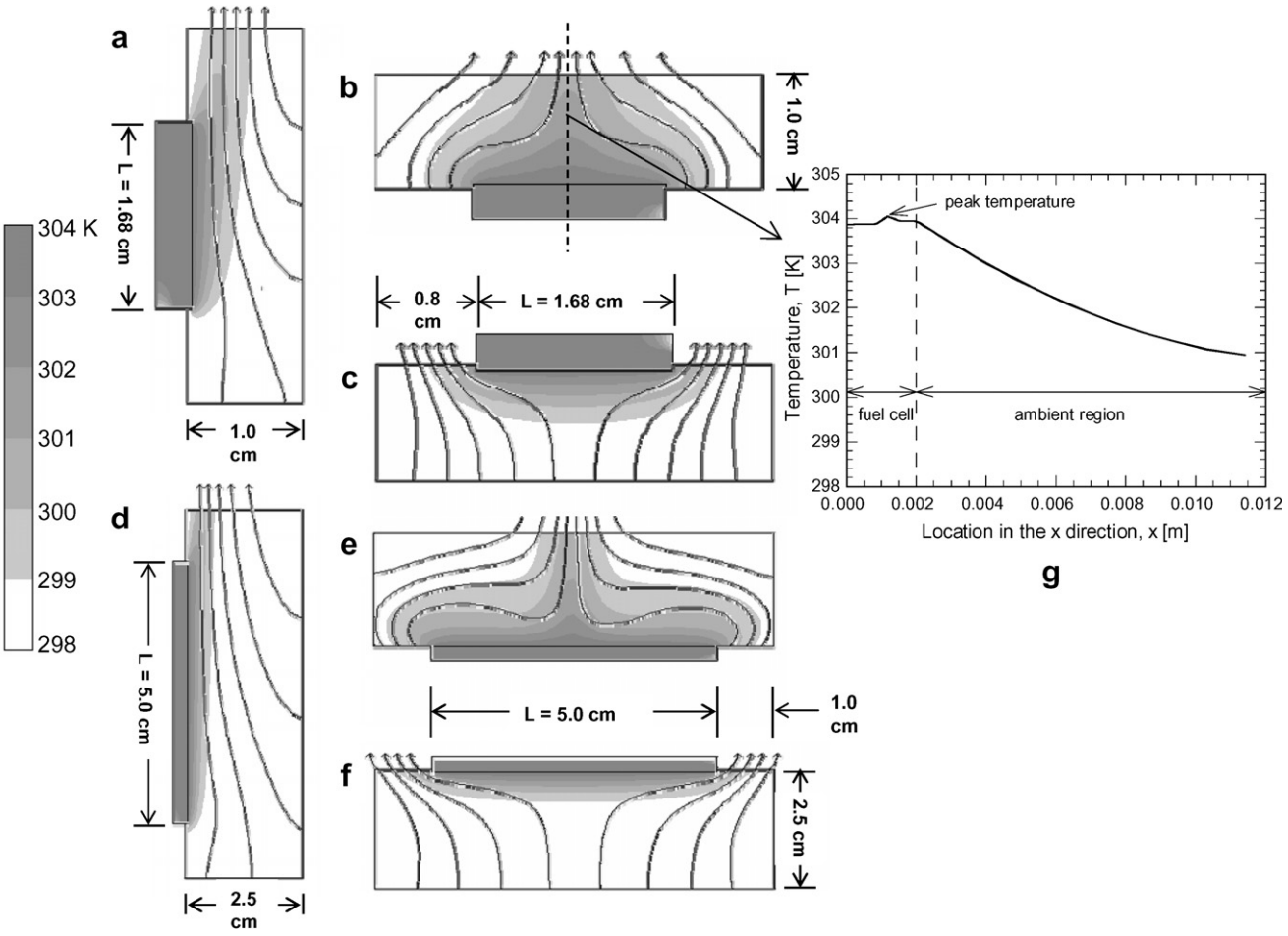

Fig. 4. Temperature distributions and flow patterns in the modeling domain for two cell lengths under three different orientations: vertical, horizontal upward and horizontal downward: (a)–(c) small cell, $L = 1.68$ cm, (d)–(f) large cell, $L = 5.0$ cm, and (g) local temperature distribution along the mid-line of the small cell, $L = 1.68$ cm.

and energy with the cell, and exhausts at the lateral sides of the cell, as seen in Fig. 4c. The same trends of temperature distributions and flow patterns are observed for the large cell in Fig. 4d–f. However, since the fuel cell size is larger, flow patterns are more concaved below the fuel cell for the horizontal downward orientation and above the fuel cell for the horizontal upward orientation in the middle of the cell length, which is also demonstrated in Ref. [38]. The flow patterns are seen to be consistent with the temperature distributions in the three orientations for both cell lengths.

Fig. 5a and b shows the polarization curves of the cell voltage E_{cell}, varying with average current density, I_{ave}, for the small cell ($L = 1.68$ cm) and the large cell ($L = 5.0$ cm), respectively, in the three orientations discussed in Fig. 4: vertical orientation, represented by the dotted line, horizontal upward, represented by the dashed line, and horizontal downward, represented by the solid line. For the small cell, Fig. 5a shows that the polarization curves for the three orientations initially overlap with one another, indicating that the cell performance at the higher cell voltages is relatively insensitive to the cell orientation. As the cell voltage is reduced to 0.4 V, the distinction starts to increase and finally the polarization curves approach different limiting current densities when the cell voltage drops to zero. In the region of cell voltage below 0.4 V, the vertical orientation provides the best cell performance, while the horizontal upward is seen to perform the worst in Fig. 5a. As illustrated in Fig. 4a and d, the flow patterns in the vertical orientation are such that cold air is drawn from the bottom and rises along the length of the cell as the air is heated by the fuel cell. In this configuration, the rising air maintains close contact with the cell surface, leading to effective oxygen absorption and water removal from the cell. On the other hand, in the horizontal upward orientation, air is drawn symmetrically from the sides, and rises away from the cell as it is heated (Fig. 4b and e). This flow pattern reduces exposure of a significant middle portion of the cell to oxygen absorption and water removal, leading to a reduced performance especially at large average current densities. Similarly, the same trend of cell performance for the large cell is presented in Fig. 5b. It is noticed that the polarization curves for the different orientations diverge earlier in the curve at a larger cell voltage of

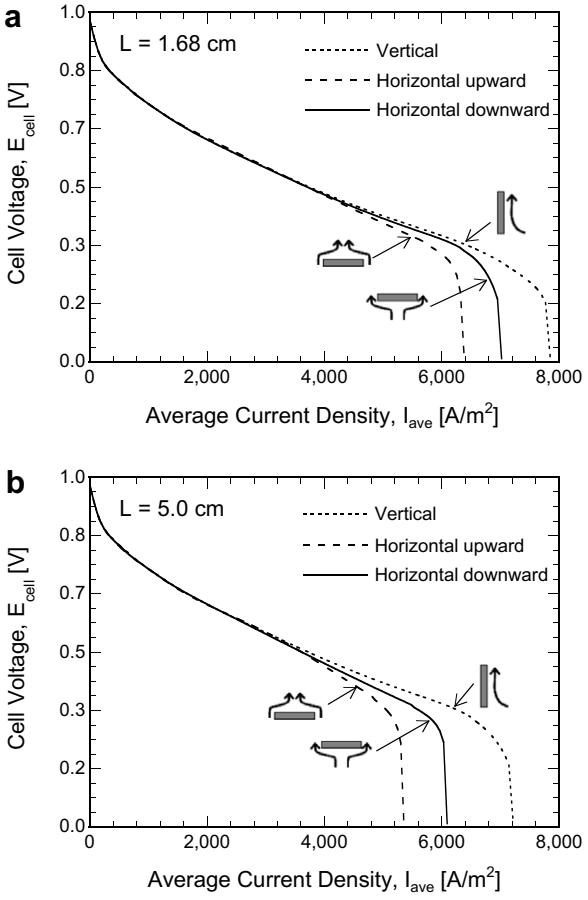

Fig. 5. The polarization curves for two cell lengths, (a) $L = 1.68$ cm, (b) $L = 5.0$ cm, under three different orientations: vertical, horizontal upward and horizontal downward.

$E_{cell} = 0.5$ V, which implies that the cell orientation is more important for air-breathing fuel cells with larger cell length, L. Furthermore, compared with Fig. 5a, the average current density, I_{ave}, at the same cell voltage, E_{cell}, decreases with increasing cell length, L, as explained in the comparison of Fig. 3a and d. However, this advantage is partly offset by the reduced active area for the smaller cells, suggesting that an optimum length may be obtained that trades off between the weight and the performance of the cell.

While Fig. 5 presented an the overview of cell performance in terms of the polarization curves, it is illustrative to examine the species distributions. Fig. 6a–c present oxygen and water mass fraction distributions at the cathode surface (i.e., surface of layer 2 in Fig. 1) along the cell length (y-direction) for a small cell ($L = 1.68$ cm) in the three orientations shown in Fig. 4a–c, respectively. Two cell voltages, $E_{cell} = 0.7$ V, denoted by the solid lines, and $E_{cell} = 0.5$ V, denoted by the dashed lines, are considered. It is seen that for all the orientations, and for all cell voltages, the oxygen mass fractions decrease initially due to oxygen consumption along the cell and then increase toward $y = L$ as fresh supply of air is available at this end of the cell. Note that for the two horizontal orientations, Fig. 6b and c, the oxygen mass fraction profile is symmetric with respect to the mid-length of the cell due to the symmetric flow pattern as seen in Fig. 4b and c and the lowest oxygen mass fraction occurs at the mid-length of the cell. The oxygen consumption is greater for the smaller cell voltage due to the increased electrochemical reactions and larger current density associated with the decreased cell voltage (Fig. 5a). The water mass fraction profiles in the three orientations are such that the largest water mass fraction occurs at the location of the smallest oxygen mass fraction since water can be easily removed from these regions owing to the flow patterns in Fig. 4.

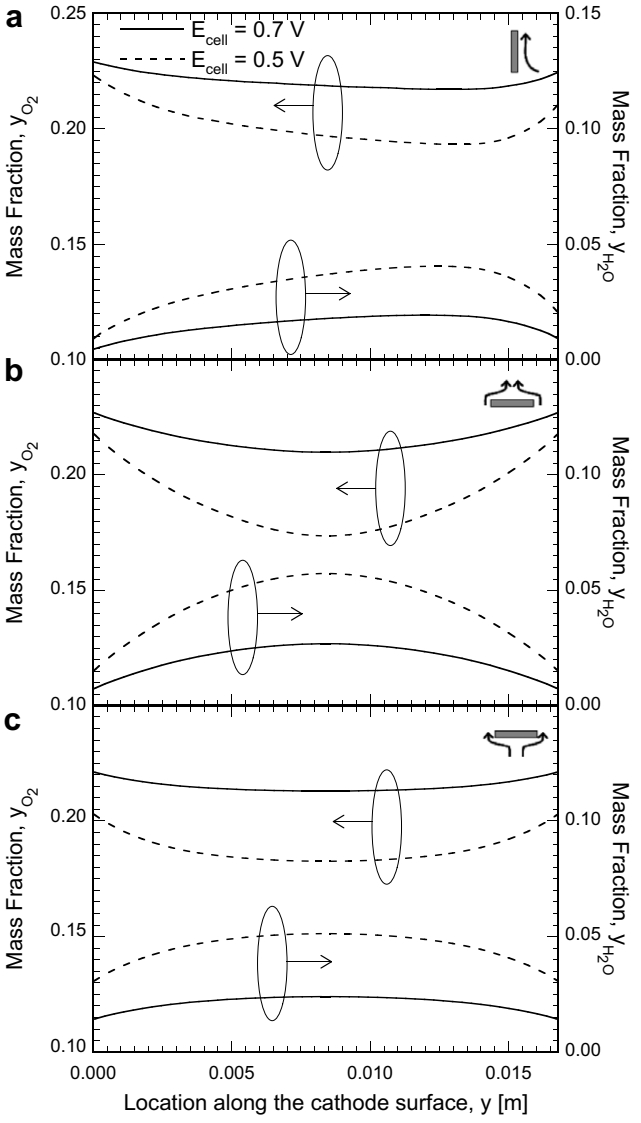

Fig. 6. Oxygen and water distributions along the cell length for the small cell ($L = 1.68$ cm) at two voltages under three different orientations: (a) vertical (b) horizontal upward, and (c) horizontal downward.

Fig. 6a–c further show that the oxygen mass fraction profile values are the largest for the vertical orientation, due to the continuous feed of fresh air, with no stagnation zones, enabled by the flow pattern depicted in Fig. 4a. The horizontal upward orientation, on the other hand, has the

lowest oxygen mass fraction values, particularly near the mid-length of the cell which is least exposed to fresh air supply, compared to other locations as well as other orientations. Furthermore, the oxygen distribution exhibits a greater variation in the horizontal upward orientation (Fig. 6b), while the variation is the smallest in the vertical orientation. Correspondingly, water mass fraction variation at the fuel cell surface is largest in the horizontal upward orientation and smallest in the vertical orientation. Water mass fraction increases with decrease of the cell voltage due to the associated large current density and enhanced electrochemical reaction, which, in turn, results in a significant variation of both oxygen and water concentration along the cell length. Similar trends in the species distributions are also seen for the large cell length of $L = 5.0$ cm in Fig. 7a–c, with two significant differences that: (a) the oxygen mass fraction is relatively smaller compared with that for the small cell (Fig. 6), (b) the oxygen mass fraction drops dramatically in the middle of the large cell, especially for the horizontal upward orientation (Fig. 7b) at low cell voltages, which indicates an extreme lack of fresh air supply at the cathode mid-length of the large cell.

Following the presentation format in Fig. 5, Fig. 8 illustrates the local current density distributions at the interface of cathode catalyst layer and the membrane along the cell length for two cell sizes in the three orientations. The shapes of the curves are similar to those of the oxygen distributions in Figs. 6 and 7 at the same orientations, which implies that the local current density distribution is primarily governed by the oxygen distribution at the cathode. The vertical orientation leads to a larger local current density and a smaller current density variation along the cell length due to the corresponding flow patterns shown in Fig. 4a and d, while the horizontal upward orientation results in the smallest local current density and the largest current density variation along the cell length.

While operating conditions at the cathode of an air-breathing cell are determined by the conditions of the ambient surrounding the cell, the operating conditions for hydrogen flow on the anode side can be varied, and it is of interest to examine the influence of the anode operat-

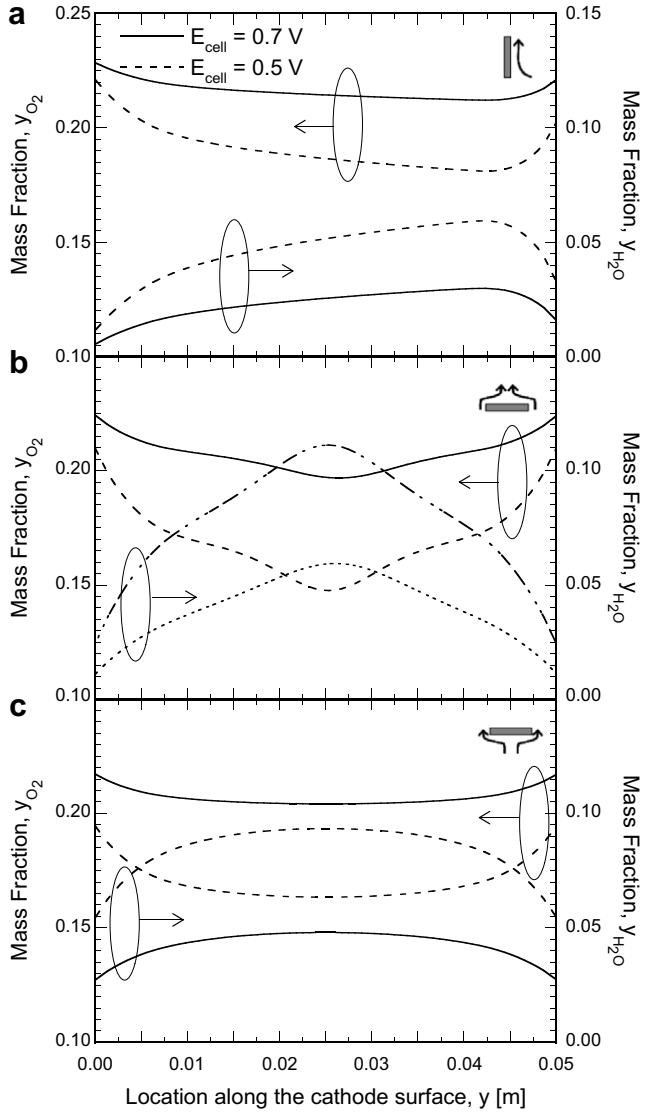

Fig. 7. Oxygen and water distributions along the cell length for the large cell ($L = 5.0$ cm) at two voltages under three different orientations: (a) vertical (b) horizontal upward, and (c) horizontal downward.

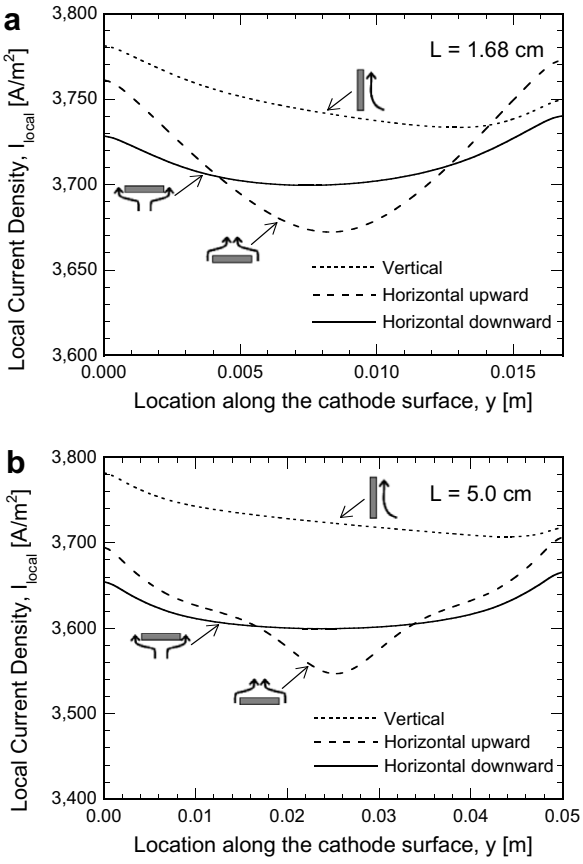

Fig. 8. Local current density distribution for two cell lengths, (a) $L = 1.68$ cm, (b) $L = 5.0$ cm, under three different orientations: vertical, horizontal upward and horizontal downward.

ing parameters on the fuel cell performance. Fig. 9 presents the effects of the anode temperature, T_a, anode pressure, p_a, anode flow rate, m_a, and anode relative humidity, RH_a, on the performance of a fuel cell of $L = 5.0$ cm. The influence of the anode temperature is shown in Fig. 9a by considering three different values of $T_a = 298$ K, 323 K and 348 K. At the larger cell voltages, increasing the temperature of hydrogen flow at the anode does not increase the cell performance significantly. The average current densities corresponding to the larger cell voltages are relatively low, and are sufficiently produced by the electrochemical reaction rate corresponding to the room temperature. Thus, an increase in the cell temperature does not improve the performance appreciably. With decrease of the cell voltage below $E_{cell} = 0.6$ V, larger current needs to be produced from the electrochemical reactions. Increasing the temperature expedites the chemical reactions and reduces the activation loss, thereby enhancing the cell performance, as seen in Fig. 9a. For a cell voltage of 0.5 V, an increase in cell temperature from 298 K to 348 K increases the current density from 3598 A/m^2 to 4805 A/m^2.

Fig. 9b demonstrates the effects of anode pressure on cell performance for three values of p_a: 1 atm, 2 atm, and 3 atm, represented by dashed line, solid line and dotted line, respectively. It is seen that the cell performance increases monotonically with increase of the anode pressure from 1 atm to 3 atm. Increasing pressure accelerates hydrogen transport through the gas diffusion layer to the catalyst region and the increased hydrogen partial pressure in the catalyst layer speeds up the reactions, in turn, reducing the reaction loss and enhancing the voltage output for a given current density. Fig. 9c presents the fuel cell performance for different hydrogen flow rates. Increasing hydrogen flow rate does not improve the cell performance significantly at the high cell voltages, where the average current density is low and the amount of hydrogen needed to produce this current density is small. Increasing the flow rate, therefore, leads to an oversupply of hydrogen without any benefit on the performance. At the low cell voltages, however, the electrochemical reactions are intense and an increased supply of hydrogen leads to enhanced current generation for a given cell voltage. For example, at a cell voltage of 0.5 V, Fig. 9c shows that the current density increases from 2830 A/m^2 to 3600 A/m^2 when the anode flow rate is doubled from 0.1 lpm to 0.2 lpm. However, with further increase in the flow rate to 0.3 lpm, the current density increases only by 280 A/m^2 to a value of 3880 A/m^2. The trend in Fig. 9c suggests that the effect of the

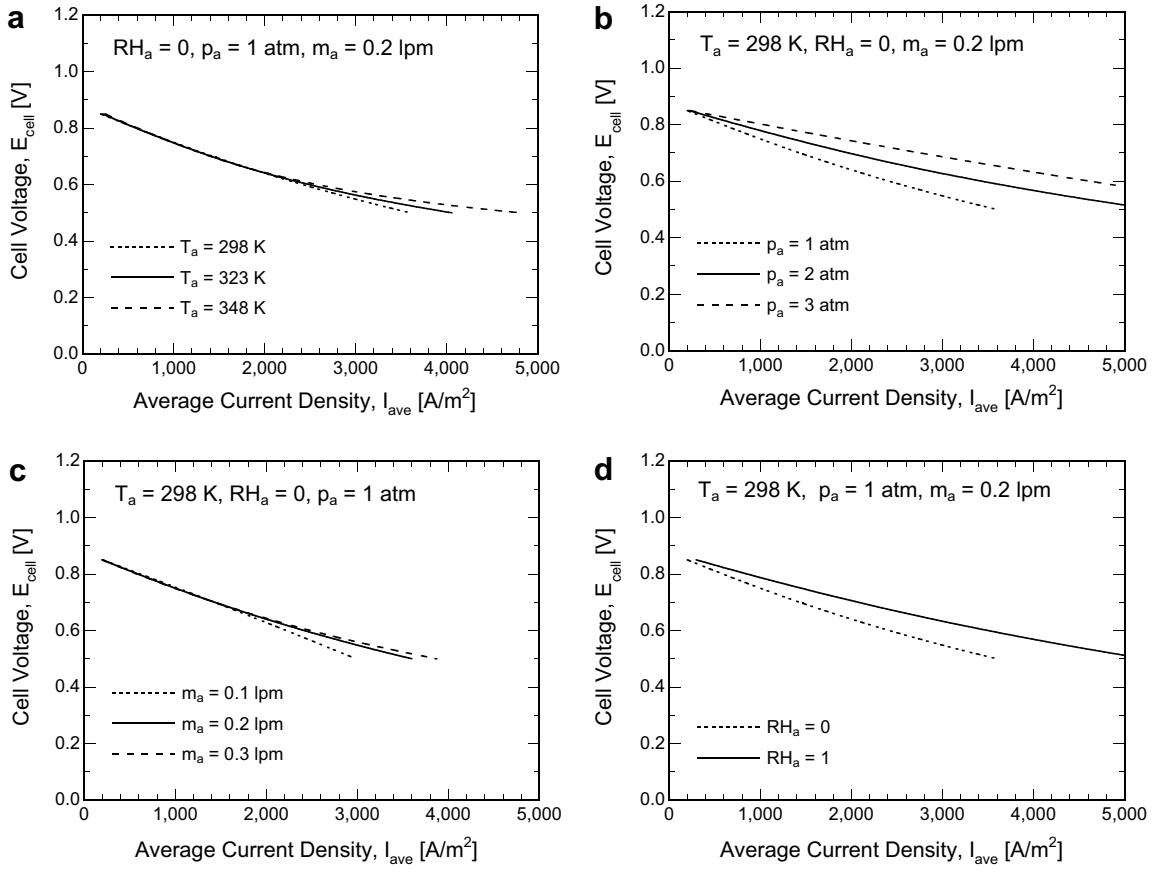

Fig. 9. Effects of the anode operating parameters, (a) anode temperature, T_a, (b) anode pressure, p_a, (c) anode flow rate, m_a, and (d) anode relative humidity, RH_a, on the polarization curve for the large cell ($L = 5.0$ cm).

anode flow rate is significant only up to a certain maximum value, and this value increases with decreasing cell voltage. Fig. 9d shows the effects of anode relative humidity on the fuel cell performance, where two conditions are considered: completely dry hydrogen, $RH_a = 0$, which eliminates the balance of plant associated with humidification and fully humidified hydrogen, $RH_a = 1$, where an external humidifier is needed. The fuel cell performance increases with the increase of anode humidity since the membrane is wet, which increases the ionic conductivity and reduces the ohmic loss. However, the fuel cell performance improvement is at the expense of the complexity of the fuel cell system.

The results in this section elucidate the performance of a new design of air breathing fuel cells of two cell lengths operating under different conditions. In a practical application, several individual cell cartridges will be configured in an array designed to deliver the target power and voltage specifications. Design of such arrays requires analysis of various configurations to arrive at optimum cell and array parameters. Computational and experimental studies on air-breathing cell arrays is reported in Ref. [40].

4. Conclusions

A two-dimensional non-isothermal steady-state computational fluid dynamics (CFD) model was presented to simulate the performance of a new design of an air-breathing PEM fuel cell. Numerical simulations were used to analyze and compare the effects of fuel cell orientation, operating conditions and geometry parameters on the cell performance. It is shown that the vertical orientation of the fuel cell leads to the largest cell performance while the horizontal upward orientation is least effective for the cell performance, especially at the low cell voltages. The studies on varying anode operating conditions including anode temperature, pressure, flow rate and relative humidity showed that increasing anode pressure and anode relative humidity significantly improves the cell performance, while the cell performance is relatively less sensitive to anode temperature and anode flow rate in the range of parameter values studied. The results further show that reducing the cell length leads to a larger local current density albeit at a loss of the active area of the cell. The analysis offers valuable physical insight towards design of a cell and a cell stack, to be considered in a future study.

Acknowledgements

The work was funded by the US Army RDECOM through Contract No. DAAB07-03-3-K-415. The authors also acknowledge Dr. Andryas Mawardi for his input.

References

[1] T.E. Springer, T.A. Zawodzinski, S. Gottesfeld, Polymer electrolyte fuel cell model, J. Electrochem. Soc. 138 (8) (1991) 2334–2342.
[2] D.M. Bernardi, M.W. Verbrugge, Mathematical model of a gas diffusion electrode bonded to a polymer electrolyte, AIChE J. 37 (8) (1991) 1151–1163.
[3] A. Rowe, X. Li, Mathematical modeling of proton exchange membrane fuel cells, J. Power Sources 102 (2001) 82–96.
[4] V. Mishra, F. Yang, R. Pitchumani, Analysis and design of PEM fuel cells, J. Power Sources 141 (2005) 47–64.
[5] A. Mawardi, F. Yang, R. Pitchumani, Optimization of the operating parameters of a proton exchange membrane fuel cell for maximum power density, ASME J. Fuel Cell Sci. Technol. 2 (2005) 121–135.
[6] V. Gurau, H. Liu, S. Kakac, Two-dimensional model for proton exchange membrane fuel cells, AIChE J. 44 (11) (1998) 2410–2422.
[7] S. Um, C.Y. Wang, K.S. Chen, Computational fluid dynamics modeling of proton exchange membrane fuel cells, J. Electrochem Soc. 147 (2000) 4485–4493.
[8] T. Zhou, H. Liu, A general three-dimensional model for proton exchange membrane fuel cells, J. Transfer Phenom. 3 (2001) 177–198.
[9] S. Dutta, S. Shimpalee, J.W. Van Zee, Numerical prediction of mass-exchange between cathode and anode channels in a PEM fuel cell, Int. J. Heat Mass Transfer 44 (2001) 2029–2042.
[10] S. Li, U. Becher, A three dimensional CFD model for PEMFC, in: Proceeding of the 2nd ASME fuel cell conference, Rochester NY, 2004.
[11] B.R. Sivertsen, N. Djilali, CFD-based modeling of proton exchange membrane fuel cells, J. Power Sources 141 (2005) 65–78.
[12] L. You, H. Liu, A two-phase flow and transport model for the cathode of PEM fuel cells, Int. J. Heat and Mass Transfer 45 (2002) 2277–2287.
[13] U. Pasaogullari, C.Y. Wang, Two-phase modeling and flooding prediction of polymer electrolyte fuel cells, J. Electrochem. Soc. 152 (2005) A380–A390.
[14] C.K. Dyer, Fuel cells for portable applications, J. Power Sources 106 (2002) 31–34.
[15] J.P. Meyers, H.L. Maynard, Design considerations for miniaturized PEM fuel cells, J. Power Sources 109 (2002) 76–88.
[16] A. Schmitz, M. Tranitz, S. Eccarius, A. Weil, C. Hebling, Influence of cathode opening size and wetting properties of diffusion layers on the performance of air-breathing PEMFCs, J. Power Sources 154 (2006) 437–447.
[17] T. Hottinen, O. Himanen, P. Lund, Effect of cathode structure on planar free breathing PEMFC, J. Power Sources 138 (2004) 205–210.
[18] F. Jaouen, S. Haasl, W. van der Wijingaart, A. Lundblad, G. Lindbergh, G. Stemme, Adhesive copper films for an air-breathing polymer electrolyte fuel cell, J. Power Sources 144 (2005) 113–121.
[19] R. Hahn, S. Wagner, A. Schmitz, H. Reichl, Development of a planar micro fuel cell with thin film and micro patterning technologies, J. Power Sources 131 (2004) 73–78.
[20] D. Modroukas, V. Modi, L.G. Frechette, Micromachined silicon structures for free-convection PEM fuel cells, J. Micromech. Microeng. 15 (2005) S193–S201.
[21] P. li, T. Zhang, Q. Wang, L. Schaefer, M.K. Chyu, The performance of PEM fuel cells fed with oxygen through the free-convection mode, J. Power Sources 114 (2003) 63–69.
[22] T. Mennola, M. Noponen, M. Aronniemi, T. Hottinen, M. Mikkola, O. Himanen, P. Lund, Mass transport in the cathode of a free-breathing polymer electrolyte membrane fuel cell, AIChE J. 33 (2003) 979–987.
[23] A. Schmitz, C. Ziegler, J.O. Schumacher, M. Tranitz, E. Fontes, C. Hebling, Modeling approach for planar self-breathing PEMFC and comparison with experimental results, Fuel Cells 4 (2004) 358–364.
[24] C. Ziegler, A. Schmitz, M. Tranitz, E. Fontes, J.O. Schumacher, Modeling planar and self-breathing fuel cells for use in electronics devices, J. Electrochem. Soc. 151 (2004) A2028–A2041.
[25] W. Ying, Y.J. Sohn, W.Y. Lee, J. Ke, C.S. Kim, Three-dimensional modeling and experimental investigation for an air-breathing polymer electrolyte membrane fuel cell (PEMFC), J. Power Sources 145 (2005) 563–571.

[26] W. Ying, T.H. Yang, W.Y. Lee, J. Ke, C.S. Kim, Three-dimensional analysis for effect of channel configuration on the performance of a small air-breathing proton exchange membrane fuel cell (PEMFC), J. Power Sources 145 (2005) 572–581.
[27] J.J. Hwang, S.D. Wu, R.G. Pen, P.Y. Chena, C.H. Chao, Mass/electron co-transports in an air-breathing cathode of a PEM fuel cell, J. Power Sources 160 (2006) 18–26.
[28] J.J. Hwang, C.H. Chao, Species-electrochemical transports in a free-breathing cathode of a PCB-based fuel cell, Electrochim. Acta 52 (2007) 1942–1950.
[29] Y. Zhang, A. Mawardi, R. Pitchumani, Effects of operating parameters on the uniformity of current density distribution in polymer electrolyte membrane (PEM) fuel cells, ASME J. Fuel Cell Sci. Technol. 3 (4) (2006) 464–476.
[30] J.J. Hwang, G.J. Hwang, R.H. Yeh, C.H. Chao, Measurement of interstitial convective heat transfer and frictional drag for flow cross metal foams, J. Heat Transfer 124 (2002) 120–129.
[31] J.J. Hwang, P.Y. Chen, Heat/mass transfer in porous electrodes of fuel cells, Int. J. Heat Mass Transfer 49 (2006) 2315–2327.
[32] J.J. Hwang, Thermal-electrochemical modeling of a proton exchange membrane fuel cell, J. Electrochem. Soc. 153 (2) (2006) A216–A224.
[33] A. Bejan, Convection Heat Transfer, second ed., John Wiley and Sons, New York, 1995, pp. 566–638.
[34] R.B. Bird, W.E. Stewart, E.N. Lightfoot, Transport Phenomena, John Wiley and Sons, New York, 2006, pp. 793–799.
[35] A. Parthasarathy, S. Srinivasan, A.J. Appleby, Temperature dependence of the electrode kinetics of oxygen reduction at the platinum/nafion interface – A microelectrode investigation, J. Electrochem. Soc. 139 (1992) 2530–2537.
[36] S.V. Patankar, Numerical Heat Transfer and Fluid Flow, Hemisphere, Washington DC, 1980, pp. 113–134.
[37] R. Pitchumani, et al., Development of portable proton exchange membrane (PEM) fuel cell hybrid system and related technologies, Technical Report AMTL-0806-01, Advanced Materials and Technologies Laboratory, University of Connecticut, CT, August 2006.
[38] F.P. Incropera, D.P. Dewitt, T. Bergman, A.S. Lavine, Fundamentals of Heat and Mass Transfer, sixth ed., John Wiley and Sons, New York, 2006, pp. 559–618.
[39] H. Ju, C.Y. Wang, Experimental validation of a PEM fuel cell model by current distribution data, J. Electrochem. Soc. 151 (11) (2004) A1954–A1960.
[40] Y. Zhang, A. Mawardi, R. Pitchumani, Numerical studies of an air-breathing proton exchange membrane (PEM) fuel cell stack, J. Power Sources, in press, doi:10.1016/j.jpowsour.2007.05.008.